Research Article

Microwave-Assisted Synthesis of Porous ZnO/SnS$_2$ Heterojunction and Its Enhanced Photoactivity for Water Purification

A. B. Makama,[1] A. Salmiaton,[1] E. B. Saion,[2] T. S. Y. Choong,[1] and N. Abdullah[1]

[1]*Department of Chemical and Environmental Engineering, Universiti Putra Malaysia (UPM), 43400 Serdang, Selangor, Malaysia*
[2]*Department of Physics, Universiti Putra Malaysia (UPM), 43400 Serdang, Selangor, Malaysia*

Correspondence should be addressed to A. Salmiaton; mie@upm.edu.my

Porous ZnO/SnS$_2$ nanocomposites with adjustable SnS$_2$ contents were prepared via microwave-assisted heating of different aqueous solutions of SnS$_2$ precursors in the presence of fixed amount of ZnCO$_3$ nanoparticles at pH 7. The structures, compositions, BET specific surface areas, and optical properties of the as-prepared products were characterized by X-ray diffraction, energy dispersive X-ray spectroscopy, transmission electron microscopy, N$_2$ adsorption, and UV-Vis absorption spectra. Photocatalytic activities of the samples were tested by the removal of aqueous ciprofloxacin, Cr^{VI}, and methylene blue under visible-light ($\lambda > 420$ nm) irradiation. The experimental results reveal that the as-prepared heterogeneous nanostructures exhibit much higher visible-light-driven photocatalytic activity for the degradation of the pollutants than pure SnS$_2$ nanocrystals. The photocatalytic degradation rates (C_t/C_0) of the pollutants for the most active heterogeneous nanostructure are about 10, 49, and 9 times higher than that of pure SnS$_2$. The enhanced photocatalytic activities exhibited by the heterojunctions could be ascribed to the synergetic effect of enhanced absorption in the visible region and the reduced rate of charge carrier recombination because of efficient separation and electron transfer from the SnS$_2$ to ZnO nanoparticles.

1. Introduction

The occurrence of subnano- to microquantities of the synthetic broad-based antibiotic ciprofloxacin (CIP) in surface and ground waters is an emerging source of high concern [1, 2]. The presence of CIP in aquatic environments, albeit at low concentrations, may lead to serious environmental issues. Of immediate concern is the high likelihood of inducing the evolution and proliferation of multidrug resistant bacteria [3]. On the mid and long term, the concern stems from not knowing the risks posed by CIP to ecosystems and human health. Because existing conventional water treatment plants are not designed to treat pharmaceutical products, there is the urgent need to develop cost-effective treatment technology to cope with this problem. In this context, advanced oxidation processes (AOPs) are being intensively investigated as possible remediation techniques. Advanced oxidation processes

hold much promise in this regard because of their ability to produce highly reactive oxidative species (ROS) that are capable of complete mineralization of recalcitrant organic, biological, and inorganic pollutants [4].

Many types of AOPs are being considered for water decontamination [5, 6]. These include electrochemical, photochemical, photocatalytic processes, or their combinations. The photochemical and electrochemical processes, such as ozonation [7, 8], photo/electro-Fenton [9, 10], and persulfate [11, 12], use expensive precursors (O$_3$, H$_2$O$_2$, and Fe^{2+} coupled with UV photons or electricity) to generate ROS. On the other hand, the photocatalytic decomposition (PCD) produces ROS without the need of any chemical and can be operated at ambient conditions. Furthermore, PCD has the inherent potential to be simple, reusable, efficient, and clean and can be designed to utilize a significant portion of the infinitely free energy from the sun. For these reasons,

PCD is widely regarded as a potentially viable AOP for water purification [13–15]. In heterogeneous photocatalytic decontamination (PCD) process, a semiconductor (SC) material harnesses energy from photons that pose energies equal to or greater than its band gap. The absorbed energy is utilized to excite electrons from the valence band to the conduction band of the semiconductor. The photogenerated electrons and holes then react with adsorbates such as O_2, H_2O to initiate the production of ROS radicals that directly degrade pollutants [16–18].

The fate and economic viability of PCD in large-scale water purification process are contingent on the development of high-performance photocatalyst(s) [19]. From industrial perspective, the optimal catalyst must possess the ability to transform the pollutant(s) entirely to harmless molecule(s). Additionally, it must have a bandgap (with suitably positioned conduction and valence bands) that absorbs light in the visible range and remains stable in contact with the water matrix. Furthermore, it should be nontoxic, abundant, and cheap. Towards this goal, a considerable variety of semiconductor materials have been tested for this purpose in the past decades. Table 1 gives a summary of some of the most recent materials investigated as photocatalysts for CIP degradation.

Among the materials under consideration are SnS_2 and ZnO semiconductors with bulk band gaps of about 2.2 eV and 3.37 eV, respectively [20]. They are among the most promising photocatalysts, owing to their low cost, nontoxic nature, and high photocatalytic activity [21–23]. Moreover, they have matched band potentials; that is, both the valence band and conduction band potentials of SnS_2 are more negative than those of ZnO [24]. Thermodynamically, this allows the photogenerated electron to easily transfer from the conduction band of SnS_2 to the conduction band of ZnO under visible-light ($\lambda > 420$ nm) irradiation, hence, enhancing the separation of photogenerated electrons and holes in SnS_2 and bringing about the sensitization of ZnO. For this reason, the ZnO/SnS_2 composites with appropriate compositions should have higher visible-light-driven photocatalytic activity than individual SnS_2 and ZnO.

On the basis of these considerations, we report a study on the synthesis of porous ZnO/SnS_2 nanosphere heterojunctions via a three-step process, including (1) room temperature synthesis of $ZnCO_3$ in polyvinyl pyrrolidone-ethylene glycol solution, (2) microwave-assisted conformal deposition of SnS_2 layer on the $ZnCO_3$ nanospheres, and (3) calcination of the $ZnCO_3$/SnS_2 nanospheres at 360°C. The objectives are to evaluate the effectiveness of porous ZnO/SnS_2 as a photocatalyst for the removal of (a) CIP and (b) hexavalent chromium ion and methylene blue. In addition, the source of enhanced photoactivity (if any) will be investigated. To the best of our knowledge, no such work on porous ZnO_3/SnS_2 was ever reported.

2. Materials and Methods

2.1. Chemicals.
All chemicals and reagents used in this work were of analytical grade and they were used as-received without any purification. The materials are ammonium hydrogen carbonate (NH_4HCO_3, Friendemann Schimdt Chemical, Germany), tin (IV) chloride pentahydrate ($SnCl_4 \cdot 5H_2O$, Acros, New Jersey, US), sodium sulfide ($Na_2S \cdot xH_2O$, QRec, Thailand), ethylene glycol ($HOCH_2CH_2OH$, Merck, Germany), zinc sulfate heptahydrate ($ZnSO_4 \cdot 7H_2O$, R & M Chemicals, UK), and polyvinyl pyrrolidone (PVP 58000, Alfa Aesar, UK), and denatured absolute ethanol (CH_3OH, Globe Chemicals, Germany). Model pollutants purchased include ciprofloxacin hydrochloride ($C_{17}H_{18}FN_3O_3$ HCl, Cadila's Ciprodac, India), potassium dichromate ($K_2Cr_2O_7$, AR grade, Systerm, Malaysia), and methylene blue (MB) whose structures and concentrations in test liquids are shown in Table 2. Distilled deionized water 18.2 mΩ·cm was prepared using TKA instrument and used to prepare all aqueous solutions.

2.2. Synthesis of $ZnCO_3$.
Zinc carbonate ($ZnCO_3$) was prepared according to an earlier reported procedure with slight modification [25]. 2.9 g (0.01 g mol) of $ZnSO_4$ (Solution A) and 1.6 g (0.02 g mol) of NH_4HCO_3 (Solution B) were each dissolved in 50 mL of 5 wt% PVP-ethylene glycol solution at 70°C. Solution B was added in a dropwise manner to Solution A under magnetic stirring at 800 rpm. The mixture was stirred for 1 h, and the white precipitate formed was collected by centrifuge at 6 000 rpm for 3 min. The precipitate was washed with distilled deionized water (3×) and then with denatured absolute ethanol (3×). Finally, the moist $ZnCO_3$ precipitate obtained was dried in an oven at 70°C for 6 h.

2.3. Microwave-Assisted Synthesis of ZnO/SnS_2.
A predetermined mass of $ZnCO_3$ powder was dispersed by sonication for 30 min in 100 mL (NaOH neutralized) solution of $SnCl_4 \cdot 5H_2O$ (pH 7) in argon sparged distilled deionized (DDI) water. After that, 20 mL solution of Na_2S also in argon sparged DDI was dropped in the $ZnCO_3$ dispersion under vigorous stirring (800 rpm). The colloidal solution under vigorous stirring was irradiated using microwave in a pulsed regime of 5 s on, 20 s off at 20% power (180 W) in an oven for 10 min. The whitish brown $ZnCO_3$/SnS_2 precipitate formed was collected by centrifuge and washed as explained in Section 2.2. The cleaned solid was calcined in a stagnant air furnace at 360°C for 3 h. Three different samples were prepared at various mass ratios of Sn^{4+} source and Zn^{2+} source that were controlled as 25, 50, and 75 wt%. Details of the experimental condition are given in Table 3. The as-prepared ZnO/SnS_2 powders are designated ZOSS-1, ZOSS-2, and ZOSS-3, respectively, and referred to as such in the text.

For the purpose of comparison, ZnO and SnS_2 were also produced in 5% PVP-EG solution using microwave heating as above.

2.4. Characterization.
Investigation of the crystallinity and the phase structures of the samples was carried out on a Phillips Analytical X-ray diffractometer. All measurements were done with Cu$_{K-\alpha}$ radiation between 2θ values of 20° and 80° at a scan rate of 0.033°s^{-1} using accelerating voltage and current of 40 mV and 40 mA, respectively. Ultraviolet-Visible (UV-Vis) absorbance spectra of samples were obtained on a

TABLE 1: Photocatalysts and experimental conditions reported for the degradation of ciprofloxacin.

Photocatalyst	Catalyst load, mg	Concentration mg/L	Radiation	Illumination time, min	CIP removal, %	References
ZnO	20	5	UV-A	60	~50	[21]
Bio MgO_x	50	10	NG^b	720	100	[52]
KMn_8O_{16}	50^a	—	NG	30	>90	[53]
Ag/Pt@TiO_2	80	10	Vis.	120	99	[54]
Ag@NC-TiO_2	80	10	Vis.	150	98	[55]
TiO_2	500	33	UV-Vis	—	—	[45]
rGO^c-$BiVO_4$	20	10	UV	60	68.2	[56]
TiO_2-P25	500	14	UV	—	—	[57]
Pt-BiO_4	150	10	Vis.	60	91.97	[58]
Anatase-TiO_2	1000	50	UV	120	—	[59]
NaCl/TiO_2	100	10	Vis.	60	70.90	[13]

^{a}Molar ratio of catalyst to CIP; ^{b}NG = not given, ^{c}rGO = reduced graphene oxide.

TABLE 2: Pollutants and some experimental conditions used in testing the photocatalytic activity of the porous ZnO/SnS_2 heterostructures. Unless otherwise indicated, reactions were performed at $(30 \pm 1)°C$ in a water-jacketed photoreactor, continuously air/argon-sparged and stirred at 400 rpm.

Model pollutant	Chemical structure	Initial concentration, mgL^{-1} ($\mu molL^{-1}$)	pH
Dichromate ion		35.5 (120.7)	5.21
Ciprofloxacin		40 (120.7)	6.10
Methylene blue		38.6 (120.7)	7.60

Shimadzu model UV-1800 spectrophotometer. Absorbance measurements are converted to absorption coefficient (α) from $\alpha = 2.303 A/d$, where d is the path length of the quartz cuvette and A is the absorbance [26, 27]. The calculated α are used in Tauc equation $[\alpha h\nu = K(h\nu - E_{bg})^n]$ to estimate the energy gap of the nanocomposite [28, 29]. Morphological structures of the samples were viewed and photographed on a Hitachi scanning electron microscope (FESEM) model S-3400N. Energy-dispersive X-ray spectrometry (EDS) was also taken on the same machine. Fine structural details were investigated with a Hitachi transmission electron microscope, model H-7100 STEM. Surface area of the samples was determined from BET measurements on a 3Flex Surface Characterization Analyzer (Micrometrics, USA). Isoelectric point (IEP) of ZOSS-2 was determined using ZetaSizer Nano ZS (Malvern, UK) instrument.

2.5. Batch Photocatalytic Activity Measurement. Photocatalytic activities of the nanocomposite were investigated by photocatalytic degradation of ciprofloxacin (CIP) in 400 mL immersion well photoreactor (model RQ400, Photochemical Reactors, UK). In a run, 200 mg of a catalyst was added to 300 mL aqueous solution of the pollutant in the reaction flask at natural pH (see Table 2). The suspension was stirred at 400 rpm for 30 min (based on preliminary contact time test result) in the dark to allow for adsorption-desorption equilibrium. Visible-light irradiation ($\lambda > 420$ nm) was generated by a 200 W quartz tungsten halogen lamp (Osram Sylvania Inc., US) which was wrapped in a UV filtering plastic sheet (F20 UV Yellow, Fluorolite Plastics, US) to remove stray UV radiation. The lamp was switched on for 10 min–15 min to reach maximum output prior to coupling to the reaction flask. After that, the light source was coupled to the reaction flask to start the photoreaction under continuous stirring at 400 rpm and O_2 supply. The lamp and reactor temperature was maintained at $(30 \pm 1)°C$ by cooling water. About 3 mL of the reaction mixture was drawn from the reactor vessel at scheduled time intervals to the maximum specified time. The

TABLE 3: Designation and summary of synthesis conditions, BET specific area, BJH pore volume, band gaps, and valence band potential of the as-synthesized specimens.

Name	[a]Zn^{2+}	[b]Sn^{4+}	Na_2S	[c]Mass	A_{BET}	BJH	E_g	E_{VB}
	mmol	mmol	mmol	%	m^2/g	cm^3/g	eV	eV
ZnO	40	0	0	0	62.7	0.823	3.3	2.9
ZOSS-1	40	3.6	7.2	25	39.4	0.571	2.9	2.2
ZOSS-2	40	7.1	14.3	50	109.1	0.767	2.8	2.1
ZOSS-3	40	10.7	21.4	75	69.7	0.229	2.6	2.0
SnS_2	0	14.3	28.5	100	19.7	0.665	2.4	2.2

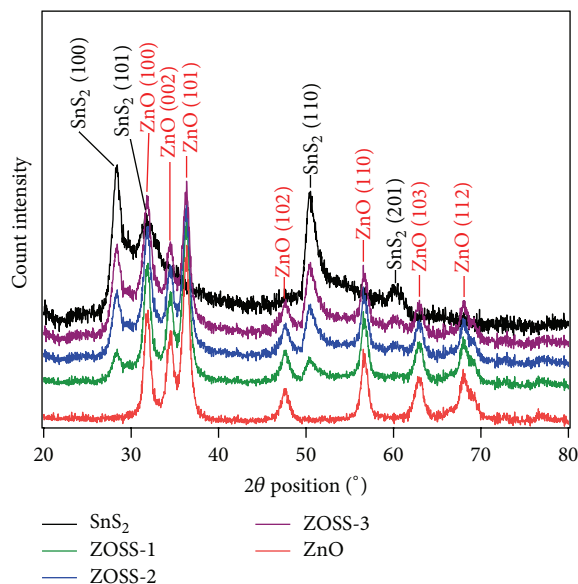[a]$ZnCO_3$; [b]$SnCl_4 \cdot 5H_2O$; [c]$SnCl_4 \cdot 5H_2O:ZnCO_3$.

FIGURE 1: XRD patterns of the as-prepared ZnO and SnS_2 and the heterojunctions.

aliquots were immediately centrifuged at 6 000 rpm for 3 min to separate the photocatalyst from the supernatant.

2.6. Analytical Methods. The temporal concentrations of the pollutants in the different supernatants were determined using established methods in the technical literature based on optical absorbance measurements. Absorbance of Cr^{VI} was taken at 540 nm according to the 1,5-diphenylcarbazide (DPC) procedure [30]. Those of CIP and MB were taken at 275 nm [31] and 664 nm, respectively. Where necessary, the absorbances were converted to concentration using calibration curves for the different pollutants.

3. Results and Discussions

3.1. Characterization of As-Synthesized Photocatalysts

3.1.1. Crystallinity and Structural. The crystalline phases of the as-prepared samples were investigated with XRD and the results are shown in Figure 1. The peaks on the diffractogram of pure ZnO could be indexed to reflections from (100), (002), (101), (102), (110), (103), and (112) planes of pure wurtzite

structure of ZnO (PDF number: 36-1451). Those on the pure SnS_2 diffractogram were indexed to the (100), (101), (110), and (201) planes of pure hexagonal phase of SnS_2 (PDF number: 23-0677). On the other hand, the diffractograms of the heterojunctions (ZOSS-1, ZOSS-2, and ZOSS-3) show peaks coming from the planes of ZnO and those of SnS_2, hence confirming that the composite powders consist of ZnO and SnS_2 phases. All the XRD patterns exhibit strong reflections and no trace of impurity peaks could be detected indicating the high crystallinity and phase purity of the products. The SnS_2 peaks on the diffractograms of ZOSS-1, ZOSS-2, and ZOSS-3 exhibit an evolutionary development with increased SnS_2 content from ZOSS-1 to ZOSS-3. The evolutionary trend is a commonly observed XRD feature of composite materials [32].

3.1.2. Surface Morphological and Elemental Analysis. The morphology and structure of ZnO, heterojunctions, and SnS_2 are photographed with SEM as shown in Figures 2(a)–2(e), respectively. The SEM images of zincite and SnS_2 in Figures 2(a) and 2(e) show that they consist of uniformly shaped and sized spherical aggregates with sizes between 0.2 μm and

(a)

(b)

(c)

(d)

(e)

(f)
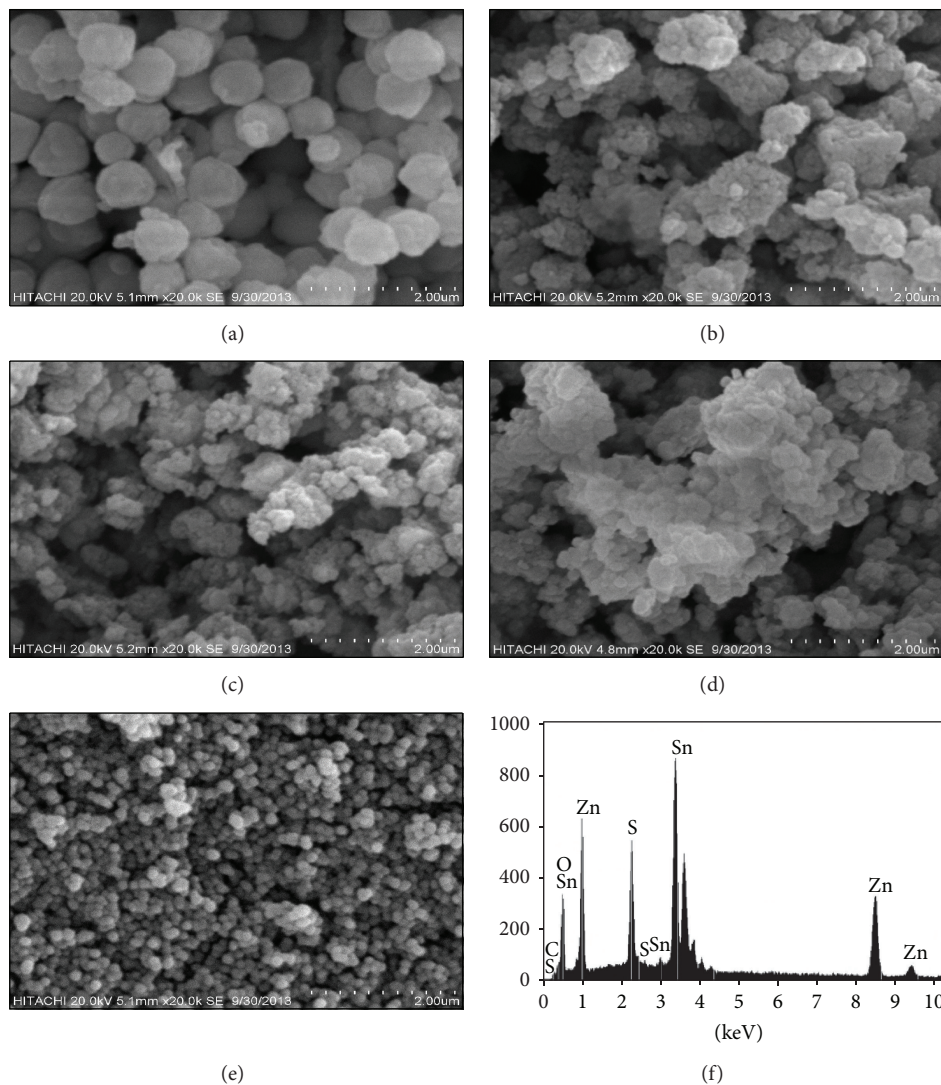
FIGURE 2: Low magnification SEM micrographs of (a) ZnO, (b) ZOSS-1, (c) ZOSS-2, (d) ZOSS-3, (e) SnS$_2$, and (f) EDX spectrum of ZOSS-2. Scale bar 2 μm.

0.8 μm. After compounding (Figures 2(b)–2(d)), the resulting composites show rough faced agglomerates that consist of spheres of ZnO covered and cemented together by mass of SnS$_2$. The degree of agglomeration increases with SnS$_2$ content from 25% to 75%. At 75%, petal like features of SnS$_2$ began to appear as shown in Figure 2(d).

The morphology of the smaller particles is further elucidated by the TEM micrograph. The TEM image of ZOSS-2 is shown in Figure 3(a). From this picture, it is clear that the ZOSS-2 heterostructure is made up of uniformly sized spheroidal particles. The dotted rectangular part in Figure 3(a) was further magnified, as shown in the inset. The enlarged portion displays that the surface of the ZnO (black spheroids) particles is entirely encased by SnS (gray mass) material. Particle size estimate obtained by counting shows the average diameter d_p of ZOSS-2 to be (10.9 ± 0.2) nm (Figure 3(b)). EDX analysis was performed to determine the elemental compositions of the ZOSS-surfaces. The analysis result for ZOSS-2 is shown on the EDX plot (Figure 2(f)), and

it further confirms the coexistence of the elements Zn, O, S, and Sn.

3.1.3. Optical Absorbance Analysis.
Optical absorbance spectral studies in the UV-Vis region were done to estimate the band gaps of the synthesized photocatalysts. Figure 4 displays the plots for pristine ZnO and SnS$_2$ and for the ZnO/SnS$_2$ (ZOSS-1 to -3) heterojunctions. It is seen that zincite exhibits no optical absorption in visible-light region due to its large energy band gap (3.3 eV). The spectra of the heterojunctions showed steep absorption over the visible-light region, indicating that the visible-light response of ZnO/SnS$_2$ materials is a manifestation of the transition between the VB and CB not from hybrid energy levels [33, 34]. The band gaps estimated from the Tauc plot (inset of Figure 4) are tabulated in Table 3. They range from 2.6 eV to 2.9 eV. The visible-light absorption abilities of the heterojunctions gradually increased with increasing SnS$_2$. The present findings seem
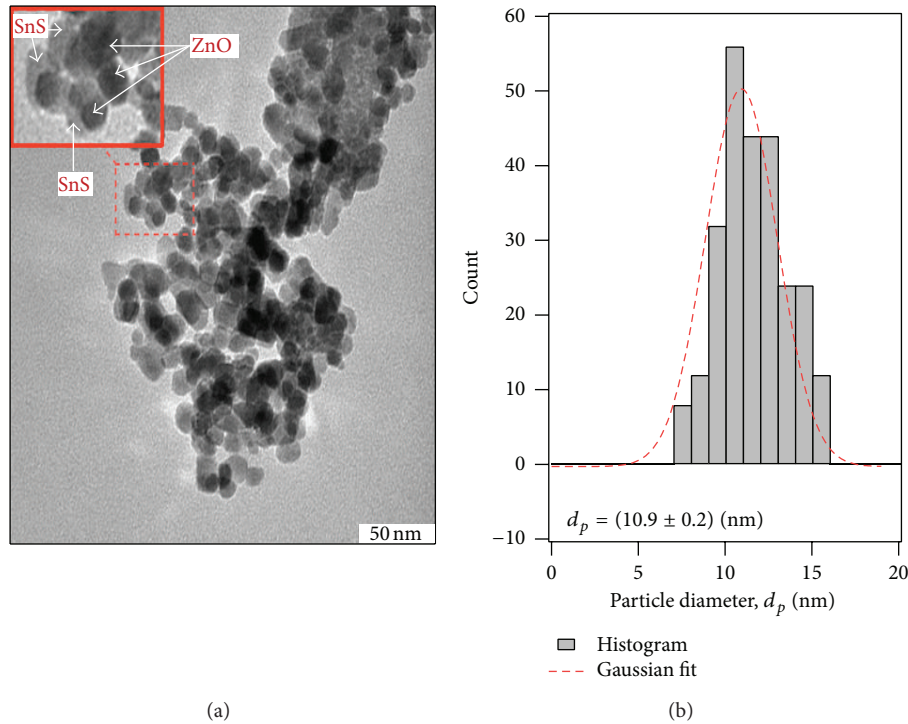
(a)

(b)

FIGURE 3: (a) TEM image and (b) particle size distribution of ZOSS-2.
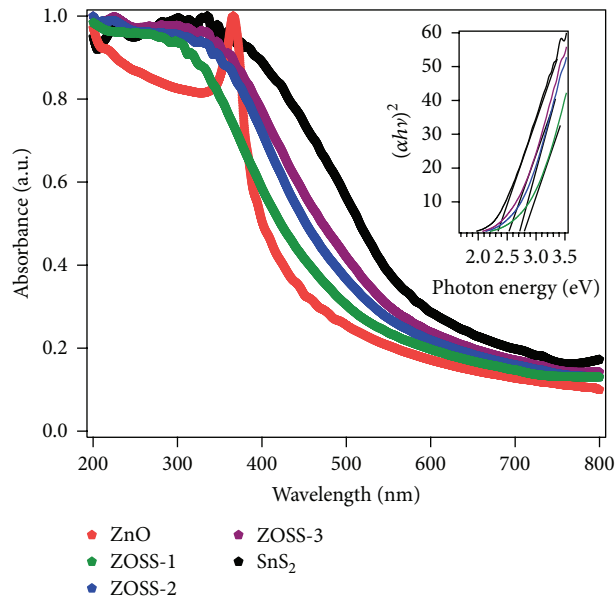

FIGURE 4: Room temperature optical absorbance spectra ZnO, ZOSS1–3, and SnS$_2$. Inset shows the Tauc ($(\alpha h\nu)^2$ versus $h\nu$) plots and band gap estimates for the SnS$_2$ and the different heterojunctions. The band gap of ZnO was estimated from the onset of absorption on the main plot.

to be consistent with other research that reported similar visible-light absorption trend of semiconductor nanocomposite materials [35].

3.1.4. Surface Area and Pore Size Distribution. The specific surface areas and pore sizes of the different photocatalysts were determined by nitrogen adsorption-desorption isotherms. The isotherms obtained revealed that all the pure phases and the heterojunctions have typical type IV isotherms according to the IUPAC classification of sorption isotherms. Figure 5(a) shows the adsorption-desorption isotherms for ZOSS-2. The isotherm with its characteristic type H1 hysteresis loop shows that the synthesized ZOSS-2 is purely a mesoporous material that contains similar sized
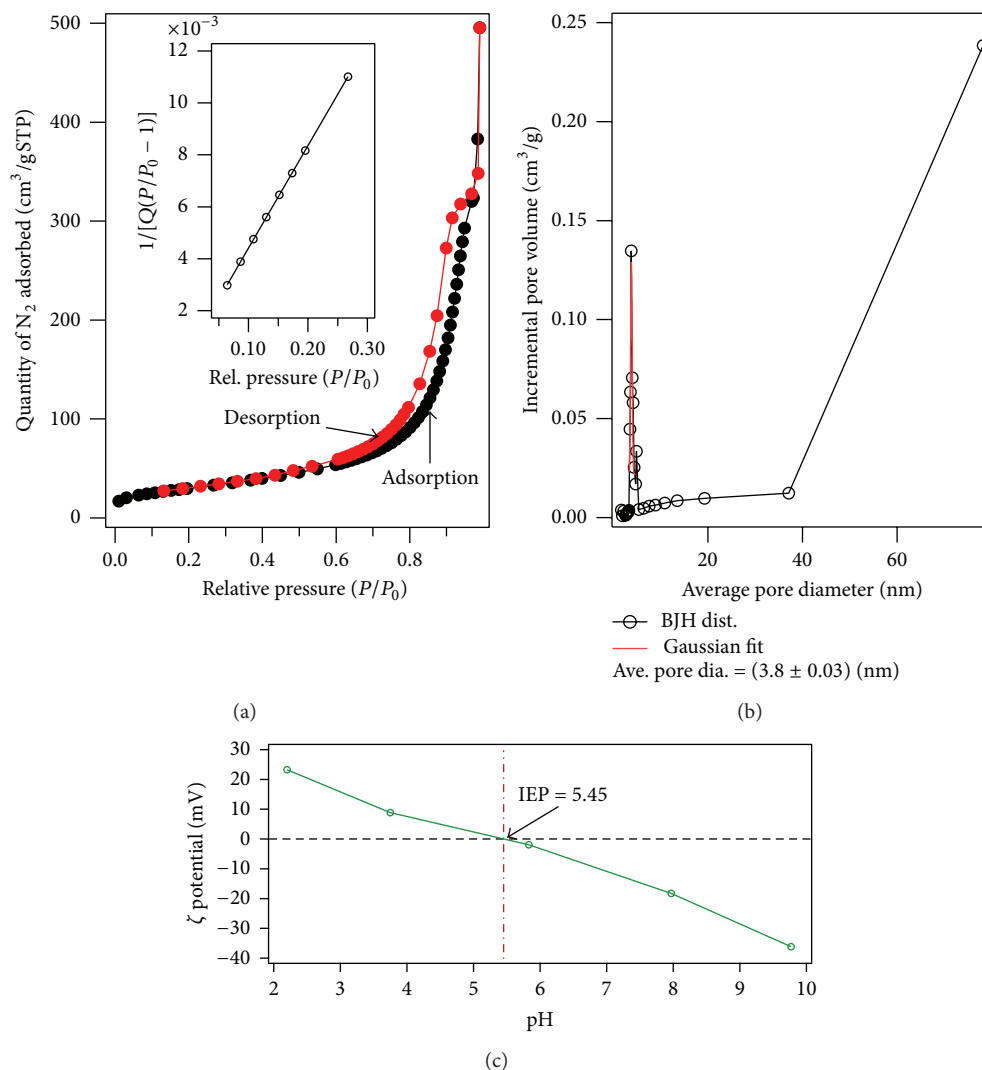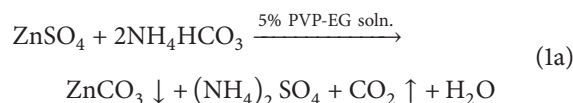
Figure 5: (a) Representative nitrogen adsorption-desorption isotherms and the BET surface area plot (inset) for ZOSS-2. (b) BJH pore size distribution. (c) ζ potential of porous ZnO/SnS$_2$ suspension as a function of pH showing the isoelectric point.

nonintersecting cylindrical mesopores [36]. The specific surface area for ZOSS-2 calculated according to the BET theory was found to be 109.1 m^{2}g^{-1}. This is much bigger than the areas of pure ZnO (62.7 m^{2}g^{-1}) and SnS$_2$ (19.7 m^{2}g^{-1}). The monolayer capacity and the BET constant of ZOSS-2 were found to be 25.1 cm^{3}g^{-1} STP and 84.5, respectively. The material also shows a moderate pore volume of 0.72 cm^{3}g^{-1}. The pore size distribution (inset of Figure 5(b)) calculated by BJH method shows that the pore diameters are in the mesoporous range with an average pore diameter equal to 3.8 nm. Similar properties for the other samples were calculated and summarized in Table 3. It is observed that the surface area increases SnS$_2$ < ZOSS-1 < ZnO < ZOSS-3 < ZOSS-2.
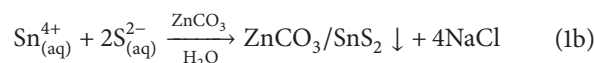
3.2. Proposed Mechanism for the Synthesis of Porous ZnO/SnS$_2$. Scheme 1 is a pictorial illustration of the

proposed steps for the formation of porous ZOSS-2 nanosphere heterojunctions.

First, uniformly shaped nanospheres of ZnCO$_3$ are produced by precipitation in 5% PVP-EG solution:

$$\text{ZnSO}_4 + 2\text{NH}_4\text{HCO}_3 \xrightarrow{\text{5\% PVP-EG soln.}}$$
$$\text{ZnCO}_3 \downarrow + (\text{NH}_4)_2 \text{SO}_4 + \text{CO}_2 \uparrow + \text{H}_2\text{O} \tag{1a}$$

Secondly, SnS$_2$ nanocrystal layer is deposited on the ZnCO$_3$ nanospheres in an aqueous solution (pH 7) to produce the ZnCO$_3$/SnS$_2$ core-shell nanospheres according to the net ionic equation:

$$\text{Sn}^{4+}_{(aq)} + 2\text{S}^{2-}_{(aq)} \xrightarrow[\text{H}_2\text{O}]{\text{ZnCO}_3} \text{ZnCO}_3/\text{SnS}_2 \downarrow + 4\text{NaCl} \tag{1b}$$
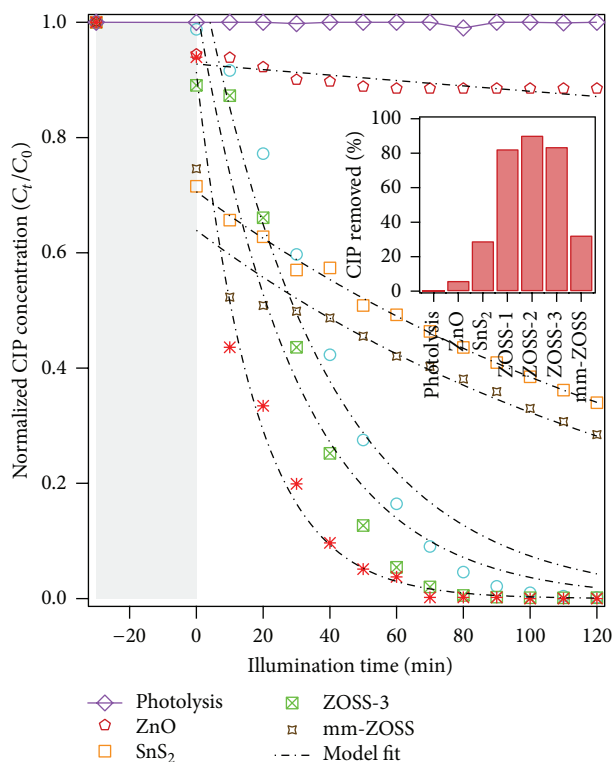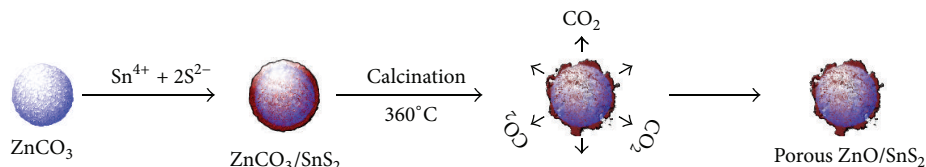
FIGURE 6: Visible-light ($\lambda > 420$ nm) induced photodegradation of CIP by photolysis and by photocatalysis over different catalysts. Inset shows the comparison of the quantity of CIP removed in 60 min by photocatalysis over the different catalysis. Rate coefficient for each reaction is tabulated in Table 4.

SCHEME 1: Schematic illustration of the conversion processes from $ZnCO_3$ nanospheres to porous ZnO/SnS_2 heterojunction.

Finally, the $ZnCO_3/SnS_2$ core-shell nanospheres are converted to porous ZnO/SnS_2 nanosphere heterojuctions by thermal decomposition at 360°C for 3 h:

$$ZnCO_3/SnS_2 \xrightarrow[360°C]{heat} \underset{porous}{ZnO/SnS_2} + CO_2 \uparrow \qquad (1c)$$

3.3. Measurement of Photocatalytic Activity

3.3.1. Degradation of Ciprofloxacin. Figure 6 shows the decay in concentration of ciprofloxacin with time as a function of photocatalysts type under visible-light. It also shows that, in the absence of the catalyst, the degradation of CIP does not occur. In the presence of the as-synthesized photocatalysts (except ZnO) however, appreciable fall in the concentrations of the pollutant was observed, indicating that the catalysts are photoactive under visible-light. The negligible activity exhibited by ZnO could be attributed to its large band gap [21] which makes it most photoactive under UV light but not

under visible-light. The percentage removal of CIP over the different catalysts in 60 min is shown as inset of Figure 6. From the figure, it is clear that the photoactivity catalysts have various activities in removing CIP. The heterojunctions (ZOSS-1–3) exhibit much higher photocatalytic activities than single phase ZnO and SnS_2. After 60 min of visible-light illumination, the CIP removal over ZnO and SnS_2 was <10% and about 30%, respectively. In contrast, the percentage decomposition in 60 min over each heterojunction was >80%. Moreover in 120 min, CIP was completely decomposed over the heterojunctions. It is worth noting that the coating of a small amount (25%) of SnS_2 on ZnO results in a sharp increase of CIP decomposition from 5.9% to 82.3% (ZOSS-1). As the SnS_2 content increases to 50% (ZOSS-2), the highest photocatalytic activity was recorded. A further increase in SnS_2 content to 75% (ZOSS-3) however results in a drop in photocatalytic activity.

The slight differences in activities of the heterojunctions under visible-light could be tied to the differences in their

SnS$_2$ content. When the content of SnS$_2$ is low as in ZOSS-1, it is very likely that a significant portion of ZnO is not covered. Thus, the visible-light response of this sample might be weak due to less SnS$_2$ content. On the other hand, more content of SnS$_2$ will result in greater SnS$_2$ coating and also lead to the development of high density of interfacial defects. Depending on the density of defects, they could either promote or impede charge carrier separation [37–39]. Low density of defects is believed to be beneficial to separation and mobility of charge carriers [40]. However, when the defects become more, they could act as electron-hole recombination centers. Consequently, electrons and holes are quenched at these centers instead of separating and thus lead to decrease of photocatalytic activity. Therefore, it is probable that the fall in activity noticed for ZOSS-3 could be ascribed to high density of charge defects as a result of more Sn^{4+} ions being incorporated into the structure of ZnO. Thus, there must exist an optimum composition for ZnO/SnS$_2$ nanocomposite to achieve the highest photocatalytic activity. For these reasons, ZOSS-2 with SnS$_2$ content of 50% possessed the highest photocatalytic activity among heterojunctions.

To evaluate the role of chemically induced interfacial binding on the photocatalytic activity of the heterojunction systems, 2 parts pure phase ZnO and 1 part pure phase SnS were mechanically mixed to produce a system with same composition as ZOSS-2 and used to photooxidized CIP under the same conditions. The activity recorded is also shown in Figure 6. The mechanically mixed specimen (mm-ZOSS) shows a rather low photocatalytic performance (32.2%) for decomposition of CIP compared to chemically produced heterojunctions. The performance of mm-ZOSS is marginally higher than the performance of the pure phase SnS$_2$ (28.2%). The low activity shown by mm-ZOSS could be explained by the relatively loose binding between the two semiconductors which hinders efficient charge transfer between them. As reported [39, 41], the main advantage of the wet synthesis of the heterojunctions is the formation of tight chemically bonded interfaces between the two materials (see Figure 3(a)). The tight binding between the two semiconductors makes charge transfer between them spatially smooth [42–44].

3.3.2. Multiactivity Test and Kinetics.

In order to better assess the activity of ZOSS-2, its performance to transform anionic (hexavalent chromium Cr^{VI}) and cationic (methylene blue (MB)) pollutant was investigated. The results of the investigation are shown in Figure 7 and they show that ZOSS-2 interacts differently with the model pollutants under dark and illuminated conditions. Under the experimental conditions tabulated in Table 2, ZOSS-2 shows excellent interaction with the pollutants. It reversely adsorbed 15.2% of Cr^{VI} from its solution and when the solution was exposed to visible-light, 81.3% of the residual Cr^{VI} was reduced to Cr^{III} in 10 min. By 20th min of illumination, the amount of Cr^{VI} was practically reduced to zero. About 6.1% of CIP was adsorbed onto ZOSS-2 and upon irradiation with light, 90.2% of the residual CIP was removed. In the case of MB, 0.2% of the dye was adsorbed after 30 min and after 60 min of irradiation, 98.2%
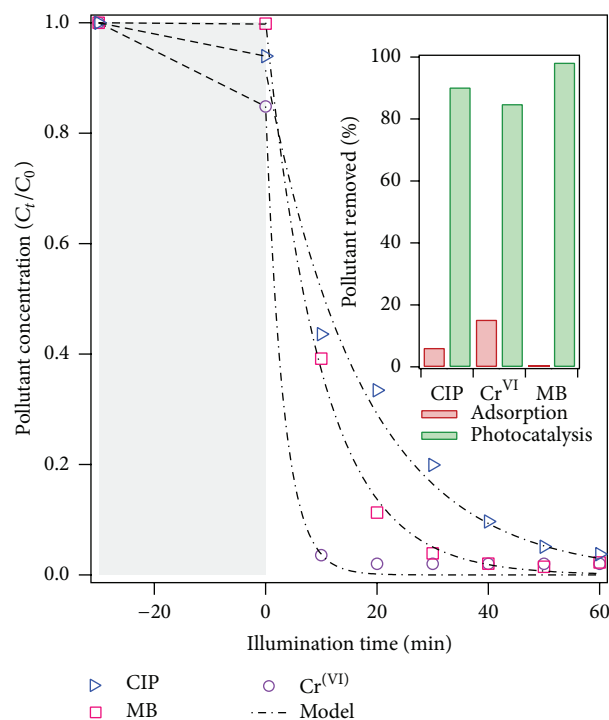

FIGURE 7: Visible-light ($\lambda > 420$ nm) photodegradation of Cr^{VI}, CIP, and MB over ZOSS-2 photocatalyst. Inset shows a comparison of CIP removed by adsorption and photocatalysis.

of the residual dye content was removed by photocatalysis. These findings show that adsorption plays only a nominal role in the transformation of the three model pollutants over ZOSS-2, suggesting that the transformation of the pollutants (especially for CIP and MB) mainly occurs in the bulk fluid, not on the catalyst surface.

To quantitatively understand the pollutants' transformation kinetics, experimental data were analyzed with the heterogeneous pseudo-first-order model as expressed by (2). The model has been applied successively [14, 16, 21, 42, 45] to represent the photocatalytic degradation process if the initial concentration of pollutant is low:

$$C_t = C_0 \exp\left(-k_r t\right), \tag{2}$$

where C_0 and C_t are the concentrations of each pollutant in solution at time 0 (optimum contact time to achieve adsorption-desorption equilibrium) and t, respectively, and k_r is the pseudo-first-order rate constant. The rate constants calculated from the nonlinear fit (NLF) of data to (2) and their corresponding χ^2 goodness of fit values for all the catalysts tested are tabulated in Table 4. A careful inspection of the χ^2-values reveals that a reasonably good fit of experimental data to the kinetic model was achieved ($\chi^2 < 0.1$). It is clearly evident from the table that the rate constants of pollutant transformation by ZOSS-2 are much higher than the other catalysts. For the same initial molar concentration of pollutants, CIP, Cr$^{(VI)}$, and MB, the rate of their removal over ZOSS-2 is about 9.2, 49, and 9 faster than by single phase SnS$_2$. The higher activity exhibited by ZOSS-2 could

TABLE 4: Pseudo-first-order rate constants and the respective chi-square test statistics of the model fit for the photocatalytic transformations of the model pollutants over the as-prepared catalysts.

Pollutant	ZnO		SnS$_2$		ZOSS-1		ZOSS-2		ZOSS-3		mm-ZOSS	
	$10^{-3}k_r$[a]	χ^2	$10^{-3}k_r$	χ^2	$10^{-3}k_r$	χ^2	$10^{-3}k_r$	χ^2	$10^{-3}k_r$	χ^2	$10^{-3}k_r$	χ^2
CIP	1.2[b]	0.0002	6.2	0.0010	27.2	0.0785	57.1	0.0102	33.3	0.0867	6.8	0.0201
Cr^{VI}	~0[c]	—	6.8	0.0003	NA[d]	NA	311.9	0.0020	NA	NA	NA	NA
MB	~0	—	10.9	0.0017	NA	NA	99.4	0.0016	NA	NA	NA	NA

[a]All k_r have units of min^{-1}; [b]see text for explanation; [c]ZnO is a large band gap semiconductor that is not active in visible-light. [d]Experiment not performed.

be attributed to its large surface area that offers more surface for visible-light absorption compared to the others. Similar findings have been reported in many reports [19, 42, 46–48]. Moreover, the dramatic increase in photoactivity of the nanocomposite is usually explained as a consequence of the formation of tight binding interface between the constituting semiconductors which favors charge carrier separation.

3.4. Apparent Quantum Yield.
A measure of the energy utilization efficiency of the reactor-photocatalyst system was assessed using the apparent quantum yield (η_{app}) concept. On the basis of time required to achieve 90% conversion level, η_{app} is defined [49] as the ratio of the rate of 90% converted molecule over the number of photons with the required energy to cause excitation of the photocatalyst that enter the reactor. Accordingly, η_{app} for the degradation of CIP can be expressed mathematically as

$$\eta_{app}^{\lambda_1 - \lambda_2} = \frac{N_{90\%}/t_{90\%}}{\left(A_{irr}/hc\right) \int_{\lambda_1}^{\lambda_2} I(\lambda) \lambda \, d\lambda}, \tag{3}$$

where $N_{90\%}$ is the number of pollutant molecules degraded at the 90% conversion level, $t_{90\%}$ is the time required to achieve 90% conversion in seconds, I (Wm^{-2}nm^{-1}) is the spectral irradiance intensity, A_{irr} (m^2) is the irradiated catalyst surface area (= 50.2 m^2), h (= 6.62×10^{-34} Js) is Plank's constant, c (= 2.997×10^8 ms^{-1}) is the speed of light in vacuum, and λ_1, λ_2 are the lower and upper wavelengths of the spectral band of interest. In this evaluation, the numerical integration of (3) is restricted within the 420 nm (λ_1)–443 nm (λ_2) spectral bandwidth for ZOSS-2. A visible high resolution spectra-photo radiometer (model BLK-HR-VIS, StellarNet Inc., US) was used to obtain the spectral distribution of the 200 W tungsten halogen lamp between 390 nm and 500 nm, as shown in Figure 8. The spectral irradiance of the lamp at the surface of outer wall of the immersion well was used to estimate the number of photons entering the reacting mixture. The apparent quantum yield was computed using (3) to be 0.225%.

3.5. Stability of the ZnO/SnS$_2$ Photocatalyst.
Although the as-synthesized ZOSS-2 heterojunction has shown excellent photocatalytic activity, this positive characteristic will amount to naught if the catalyst is not stable for repeat operation. For this reason, its stability was investigated by recycling it over and over in the decomposition of CIP under visible-light. Before any new cycle of the experimental run, the
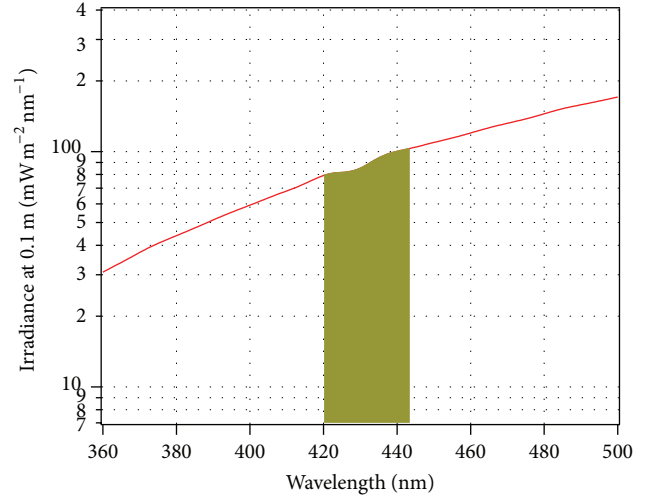

FIGURE 8: Spectral irradiance of the 200 W tungsten halogen lamp measured at the outer wall of the immersion wall ($\approx$ 10.0 cm away from the lamp). Shaded area represents the spectral band of interest.

used catalyst was first cleaned, dried, and weighed. The result of the stability test is shown in Figure 9 and from it, it is apparent that there is very little lost in the activity of the ZOSS-2 photocatalyst after the first five reuse cycles. From this finding, it can be supposed that, under the current set of experimental conditions, ZOSS-2 is a stable photocatalyst.

3.6. Charge Transfer between the SnS$_2$ and ZnO Crystals and Enhancement of Photocatalytic Activity of ZnO/SnS$_2$.
It is widely believed [19, 35, 39, 44] that the much better performance exhibited by composite semiconductor photocatalysts over single phase materials is mainly due to the phenomenon of electric-field-assisted photon induced charge separation and transfer across the systems' boundary. Thus, in order to understand the charge separation process between SnS$_2$ and ZnO interface, the valence band (VB) and conduction band (CB) potentials at the point of zero charge were calculated according to the electronegativity concept [50] using the empirical equations

$$E_{VB} = \psi - E^e + 0.5E_g, \tag{4a}$$

$$E_{CB} = E_{VB} - E_g, \tag{4b}$$

where ψ is the absolute electronegativity of the semiconductor, which is defined as the geometric mean of the absolute electronegativity of the constituent atoms. The absolute
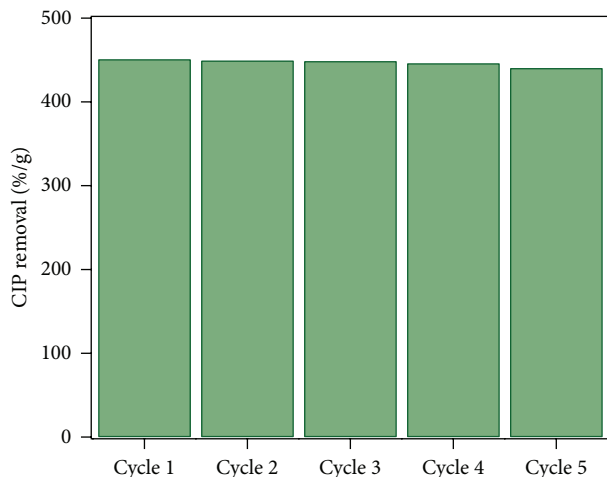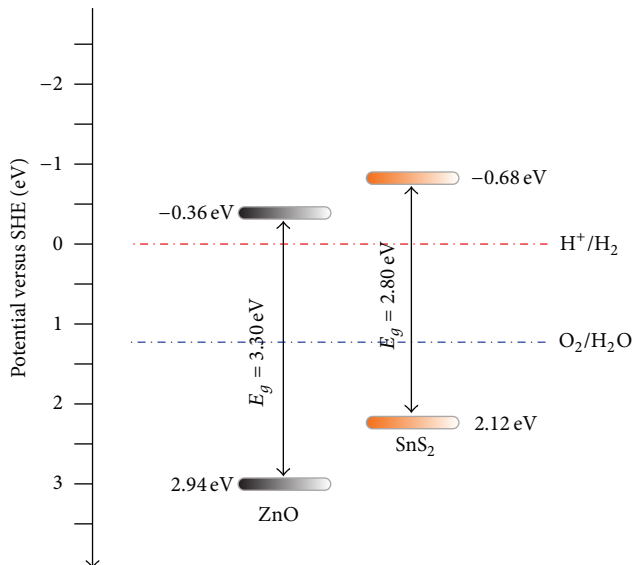
FIGURE 9: Photocatalytic performances of ZnO/SnS$_2$ in the first five reuse cycles.

SCHEME 2: Electronic band diagram of the ZnO/SnS$_2$ system.

electrons in the CB of SnS$_2$ crystal can readily move across the system boundary to the CB of ZnO. At the other end, the holes (h$^+$) created as a result of photon excitation of electrons remain in the VB of SnS$_2$ because it is at a lower potential than the VB of ZnO. In addition, the separation of electron-hole pairs is also aided by the internal electric fields generated within the depletion region of the two semiconductors. In other words, the small built-in voltage also induces the separation of electron-hole pairs both at the interface and in the individual semiconductors [43]. This also helps to reduce the probability of electron-hole recombination within the crystals. As a result, electrons are localized on the ZnO surface and holes on the SnS$_2$ surface. The separation and localization of electrons and holes in different semiconductors could effectively inhibit their recombination. Consequently, the lifetimes of these charge carriers are prolonged. This gives them the higher probability to partake in redox reactions which manifests as increased activity for the heterojunctions [42, 48].

4. Conclusions

Porous ZnO/SnS$_2$ heterostructures were synthesized through simple microwave-assisted heating chemical method at pH 7. The presence of SnS$_2$ extended the spectral response of ZnO from the UV to the visible region, enabling the heterostructures to efficiently remove ciprofloxacin, hexavalent chromium, and methylene blue from aqueous solutions under visible-light irradiation. The characterization results confirmed the formation of heterojunction and revealed that the heterojunction could promote the transfer of photoelectrons and thus inhibit their recombination with holes, leading to enhanced photocatalytic activity. The study suggests that the porous ZnO/SnS$_2$ heterostructures are new types of visible-light-driven photocatalysts for environmental applications.

Conflict of Interests

The authors declare that there is no conflict of interests regarding the publication of this paper.

Acknowledgments

References

[1] M. Gros, M. Petrović, and D. Barceló, "Tracing pharmaceutical residues of different therapeutic classes in environmental waters by using liquid chromatography/quadrupole-linear ion trap mass spectrometry and automated library searching," *Analytical Chemistry*, vol. 81, no. 3, pp. 898–912, 2009.

[2] T. Christian, R. J. Schneider, H. A. Färber, D. Skutlarek, M. T. Meyer, and H. E. Goldbach, "Determination of antibiotic

electronegativity of the constituent atoms is defined as the arithmetic mean of the atomic electron affinity and the first ionization energy. The ψ values for SnS$_2$ and ZnO were calculated with data from Pearson [51] to be 5.17 eV and 5.79 eV, respectively. E^e is the energy of free electrons on the hydrogen scale (ca. 4.5 eV) and E_g is the band gap of the semiconductor. The E_g values for ZnO and SnS$_2$ obtained in the experiments are 3.3 eV and 2.4 eV, respectively. Accordingly, the VB and CB energy values of SnS$_2$ crystals were calculated to be 1.87 eV and −0.53 eV while those for ZnO crystals were determined to be 2.89 eV and −0.36 eV, respectively.

Using the computed band potentials, the electronic band diagram of the heterojunction is drawn and shown in Scheme 2. As seen from the scheme, the ZnO/SnS$_2$ heterojunction is a "staggered" type II system. The CB edge potential of SnS$_2$ (−0.53 eV) is at a more negative potential than that of ZnO (−0.36 eV). Hence, visible-light excited

residues in manure, soil, and surface waters," *Acta Hydrochimica et Hydrobiologica*, vol. 31, no. 1, pp. 36–44, 2003.

[3] Z. Liu, P. Sun, S. G. Pavlostathis, X. Zhou, and Y. Zhang, "Adsorption, inhibition, and biotransformation of ciprofloxacin under aerobic conditions," *Bioresource Technology*, vol. 144, pp. 644–651, 2013.

[4] C. Comninellis, A. Kapalka, S. Malato, S. A. Parsons, I. Poulios, and D. Mantzavinos, "Advanced oxidation processes for water treatment: advances and trends for R&D," *Journal of Chemical Technology and Biotechnology*, vol. 83, no. 6, pp. 769–776, 2008.

[5] L. Feng, E. D. van Hullebusch, M. A. Rodrigo, G. Esposito, and M. A. Oturan, "Removal of residual anti-inflammatory and analgesic pharmaceuticals from aqueous systems by electrochemical advanced oxidation processes. A review," *Chemical Engineering Journal*, vol. 228, pp. 944–964, 2013.

[6] J. Rivera-Utrilla, M. Sánchez-Polo, M. Á. Ferro-García, G. Prados-Joya, and R. Ocampo-Pérez, "Pharmaceuticals as emerging contaminants and their removal from water. A review," *Chemosphere*, vol. 93, no. 7, pp. 1268–1287, 2013.

[7] C. Liu, V. Nanaboina, G. V. Korshin, and W. Jiang, "Spectroscopic study of degradation products of ciprofloxacin, norfloxacin and lomefloxacin formed in ozonated wastewater," *Water Research*, vol. 46, no. 16, pp. 5235–5246, 2012.

[8] T. G. Vasconcelos, K. Kümmerer, D. M. Henriques, and A. F. Martins, "Ciprofloxacin in hospital effluent: degradation by ozone and photoprocesses," *Journal of Hazardous Materials*, vol. 169, no. 1–3, pp. 1154–1158, 2009.

[9] S. Miralles-Cuevas, A. Arqués, M. I. Maldonado, J. A. Sánchez-Pérez, and S. Malato Rodríguez, "Combined nanofiltration and photo-Fenton treatment of water containing micropollutants," *Chemical Engineering Journal*, vol. 224, no. 1, pp. 89–95, 2013.

[10] M. S. Yahya, N. Oturan, K. El Kacemi, M. El Karbane, C. Aravindakumar, and M. A. Oturan, "Oxidative degradation study on antimicrobial agent ciprofloxacin by electro-fenton process: kinetics and oxidation products," *Chemosphere*, vol. 117, pp. 447–454, 2014.

[11] M. Mahdi-Ahmed and S. Chiron, "Ciprofloxacin oxidation by UV-C activated peroxymonosulfate in wastewater," *Journal of Hazardous Materials*, vol. 265, pp. 41–46, 2014.

[12] Y. Ji, C. Ferronato, A. Salvador, X. Yang, and J.-M. Chovelon, "Degradation of ciprofloxacin and sulfamethoxazole by ferrous-activated persulfate: implications for remediation of groundwater contaminated by antibiotics," *Science of the Total Environment*, vol. 472, pp. 800–808, 2014.

[13] X. Liu, P. Lv, G. Yao et al., "Selective degradation of ciprofloxacin with modified NaCl/TiO$_2$ photocatalyst by surface molecular imprinted technology," *Colloids and Surfaces A: Physicochemical and Engineering Aspects*, vol. 441, pp. 420–426, 2014.

[14] J. Ryu and W. Choi, "Substrate-specific photocatalytic activities of TiO$_2$ and multiactivity test for water treatment application," *Environmental Science and Technology*, vol. 42, no. 1, pp. 294–300, 2008.

[15] H. Zhao, H.-J. Cui, and M.-L. Fu, "Synthesis of core-shell structured Fe$_3$O$_4$@α-MnO$_2$ microspheres for efficient catalytic degradation of ciprofloxacin," *RSC Advances*, vol. 4, no. 74, pp. 39472–39475, 2014.

[16] U. I. Gaya and A. H. Abdullah, "Heterogeneous photocatalytic degradation of organic contaminants over titanium dioxide: a review of fundamentals, progress and problems," *Journal of Photochemistry and Photobiology C: Photochemistry Reviews*, vol. 9, no. 1, pp. 1–12, 2008.

[17] J.-M. Herrmann, C. Guillard, and P. Pichat, "Heterogeneous photocatalysis: an emerging technology for water treatment," *Catalysis Today*, vol. 17, no. 1-2, pp. 7–20, 1993.

[18] A. Houas, H. Lachheb, M. Ksibi, E. Elaloui, C. Guillard, and J.-M. Herrmann, "Photocatalytic degradation pathway of methylene blue in water," *Applied Catalysis B: Environmental*, vol. 31, no. 2, pp. 145–157, 2001.

[19] Y. C. Zhang, J. Li, and H. Y. Xu, "One-step in situ solvothermal synthesis of SnS$_2$/TiO$_2$ nanocomposites with high performance in visible light-driven photocatalytic reduction of aqueous Cr(VI)," *Applied Catalysis B: Environmental*, vol. 123-124, pp. 18–26, 2012.

[20] B. Ghosh, M. Das, P. Banerjee, and S. Das, "Fabrication of the SnS/ZnO heterojunction for PV applications using electrodeposited ZnO films," *Semiconductor Science and Technology*, vol. 24, no. 2, Article ID 025024, 2009.

[21] M. El-Kemary, H. El-Shamy, and I. El-Mehasseb, "Photocatalytic degradation of ciprofloxacin drug in water using ZnO nanoparticles," *Journal of Luminescence*, vol. 130, no. 12, pp. 2327–2331, 2010.

[22] Y. C. Zhang, J. Li, M. Zhang, and D. D. Dionysiou, "Size-tunable hydrothermal synthesis of SnS$_2$ nanocrystals with high performance in visible light-driven photocatalytic reduction of aqueous Cr(VI)," *Environmental Science and Technology*, vol. 45, no. 21, pp. 9324–9331, 2011.

[23] F. Liu, Y. H. Leung, A. B. Djurišić, A. M. C. Ng, and W. K. Chan, "Native defects in zno: effect on dye adsorption and photocatalytic degradation," *Journal of Physical Chemistry C*, vol. 117, no. 23, pp. 12218–12228, 2013.

[24] Y. Xu and M. A. Schoonen, "The absolute energy positions of conduction and valence bands of selected semiconducting minerals," *American Mineralogist*, vol. 85, no. 3-4, pp. 543–556, 2000.

[25] R. Zhang, F. Zhang, J. Feng, and Y. Qian, "Green and facile synthesis of porous ZnCO$_3$ as a novel anode material for advanced lithium-ion batteries," *Materials Letters*, vol. 118, pp. 5–7, 2014.

[26] J. Sancho-Parramon, V. Janicki, and H. Zorc, "Compositional dependence of absorption coefficient and band-gap for Nb$_2$O$_5$-SiO$_2$ mixture thin films," *Thin Solid Films*, vol. 516, no. 16, pp. 5478–5482, 2008.

[27] E. A. Davis and N. F. Mott, "Conduction in non-crystalline systems V. Conductivity, optical absorption and photoconductivity in amorphous semiconductors," *Philosophical Magazine*, vol. 22, no. 179, pp. 0903–0922, 1970.

[28] A. B. Murphy, "Band-gap determination from diffuse reflectance measurements of semiconductor films, and application to photoelectrochemical water-splitting," *Solar Energy Materials and Solar Cells*, vol. 91, no. 14, pp. 1326–1337, 2007.

[29] J. Tauc and A. Menth, "States in the gap," *Journal of Non-Crystalline Solids*, vol. 8–10, pp. 569–585, 1972.

[30] A. D. Eaton, APHA, AWWA, and WEF, *Standard Methods for the Examination of Water and Wastewater*, APHA-AWWA-WEF, Washington, DC, USA, 20th edition, 1999.

[31] Y. Sun, Q. Yue, B. Gao et al., "Adsorption and cosorption of ciprofloxacin and Ni(II) on activated carbon-mechanism study," *Journal of the Taiwan Institute of Chemical Engineers*, vol. 45, no. 2, pp. 681–688, 2014.

[32] J. Luo, L. Ma, T. He et al., "TiO$_2$/(CdS, CdSe, CdSeS) nanorod heterostructures and photoelectrochemical properties," *Journal of Physical Chemistry C*, vol. 116, no. 22, pp. 11956–11963, 2012.

[33] A. Kudo, "Photocatalyst materials for water splitting," *Catalysis Surveys from Asia*, vol. 7, no. 1, pp. 31–38, 2003.

[34] Z. Lei, W. You, M. Liu et al., "Photocatalytic water reduction under visible light on a novel $ZnIn_2S_4$ catalyst synthesized by hydrothermal method," *Chemical Communications*, vol. 9, no. 17, pp. 2142–2143, 2003.

[35] G. Yang, B. Yang, T. Xiao, and Z. Yan, "One-step solvothermal synthesis of hierarchically porous nanostructured CdS/TiO_2 heterojunction with higher visible light photocatalytic activity," *Applied Surface Science*, vol. 283, pp. 402–410, 2013.

[36] K. S. W. Sing, D. Everet, R. Haul et al., "Reporting physisorption data for gas/solid systems with special reference to the determination of surface area and porosity (recomendations1984)," *Pure and Applied Chemistry*, vol. 54, no. 11, pp. 2201–2218, 1982.

[37] H.-Y. Chen and D. H. Son, "Energy and charge transfer dynamics in doped semiconductor nanocrystals," *Israel Journal of Chemistry*, vol. 52, no. 11-12, pp. 1016–1026, 2012.

[38] A. Kudo, "Recent progress in the development of visible light-driven powdered photocatalysts for water splitting," *International Journal of Hydrogen Energy*, vol. 32, no. 14, pp. 2673–2678, 2007.

[39] X. Lin, J. Xing, W. Wang, Z. Shan, F. Xu, and F. Huang, "Photocatalytic activities of heterojunction semiconductors $Bi_2O_3/BaTiO_3$: a strategy for the design of efficient combined photocatalysts," *The Journal of Physical Chemistry C*, vol. 111, no. 49, pp. 18288–18293, 2007.

[40] L. Yang, C.-W. Cheng, M. T. Bulsara, and E. A. Fitzgerald, "High mobility $In_{0.53}Ga_{0.47}As$ quantum-well metal oxide semiconductor field effect transistor structures," *Journal of Applied Physics*, vol. 111, no. 10, Article ID 104511, 2012.

[41] J. Li, T. Wang, and X. Du, "Preparation of visible light-driven SnS_2/TiO_2 nanocomposite photocatalyst for the reduction of aqueous Cr(VI)," *Separation and Purification Technology*, vol. 101, pp. 11–17, 2012.

[42] W. Wang, J. Wang, Z. Wang et al., "p-n junction $CuO/BiVO_4$ heterogeneous nanostructures: synthesis and highly efficient visible-light photocatalytic performance," *Dalton Transactions*, vol. 43, no. 18, pp. 6735–6743, 2014.

[43] W. Wang, F. Huang, and X. Lin, "xBiOI-(1-x)BiOCl as efficient visible-light-driven photocatalysts," *Scripta Materialia*, vol. 56, no. 8, pp. 669–672, 2007.

[44] X. Zhang, L. Zhang, T. Xie, and D. Wang, "Low-temperature synthesis and high visible-light-induced photocatalytic activity of $BiOI/TiO_2$ heterostructures," *Journal of Physical Chemistry C*, vol. 113, no. 17, pp. 7371–7378, 2009.

[45] T. Paul, P. L. Miller, and T. J. Strathmann, "Visible-light-mediated TiO_2 photocatalysis of fluoroquinolone antibacterial agents," *Environmental Science and Technology*, vol. 41, no. 13, pp. 4720–4727, 2007.

[46] M. Farbod and M. Kajbafvala, "Effect of nanoparticle surface modification on the adsorption-enhanced photocatalysis of Gd/TiO_2 nanocomposite," *Powder Technology*, vol. 239, pp. 434–440, 2013.

[47] A. Franco, M. C. Neves, M. M. L. R. Carrott, M. H. Mendonça, M. I. Pereira, and O. C. Monteiro, "Photocatalytic decolorization of methylene blue in the presence of TiO_2/ZnS nanocomposites," *Journal of Hazardous Materials*, vol. 161, no. 1, pp. 545–550, 2009.

[48] W. Li, X. Cui, P. Wang, Y. Shao, D. Li, and F. Teng, "Enhanced photosensitized degradation of rhodamine B on CdS/TiO_2 nanocomposites under visible light irradiation," *Materials Research Bulletin*, vol. 48, no. 9, pp. 3025–3031, 2013.

[49] H. Ibrahim and H. de Lasa, "Photo-catalytic degradation of air borne pollutants apparent quantum efficiencies in a novel photo-CREC-air reactor," *Chemical Engineering Science*, vol. 58, no. 3-6, pp. 943–949, 2003.

[50] M. A. Butler and D. S. Ginley, "Prediction of flatband potentials at semiconductor-electrolyte interfaces from atomic electronegativities," *Journal of the Electrochemical Society*, vol. 125, no. 2, pp. 228–232, 1978.

[51] R. G. Pearson, "Absolute electronegativity and hardness: application to inorganic chemistry," *Inorganic Chemistry*, vol. 27, no. 4, pp. 734–740, 1988.

[52] J. Tu, Z. Yang, C. Hu, and J. Qu, "Characterization and reactivity of biogenic manganese oxides for ciprofloxacin oxidation," *Journal of Environmental Sciences*, vol. 26, no. 5, pp. 1154–1161, 2014.

[53] X. Xiao, S.-P. Sun, M. B. McBride, and A. T. Lemley, "Degradation of ciprofloxacin by cryptomelane-type manganese(III/IV) oxides," *Environmental Science and Pollution Research*, vol. 20, no. 1, pp. 10–21, 2013.

[54] Z. Jiang, J. Zhu, D. Liu, W. Wei, J. Xie, and M. Chen, "*In situ* synthesis of bimetallic Ag/Pt loaded single-crystalline anatase TiO_2 hollow nano-hemispheres and their improved photocatalytic properties," *CrystEngComm*, vol. 16, no. 12, pp. 2384–2394, 2014.

[55] Z. Jiang, X. Lv, D. Jiang, J. Xie, and D. Mao, "Natural leaves-assisted synthesis of nitrogen-doped, carbon-rich nanodots-sensitized, Ag-loaded anatase TiO_2 square nanosheets with dominant 001 facets and their enhanced catalytic applications," *Journal of Materials Chemistry A*, vol. 1, no. 47, pp. 14963–14972, 2013.

[56] Y. Yan, S. Sun, Y. Song et al., "Microwave-assisted in situ synthesis of reduced graphene oxide-$BiVO_4$ composite photocatalysts and their enhanced photocatalytic performance for the degradation of ciprofloxacin," *Journal of Hazardous Materials*, vol. 250-251, pp. 106–114, 2013.

[57] X. van Doorslaer, K. Demeestere, P. M. Heynderickx, H. van Langenhove, and J. Dewulf, "UV-A and UV-C induced photolytic and photocatalytic degradation of aqueous ciprofloxacin and moxifloxacin: reaction kinetics and role of adsorption," *Applied Catalysis B: Environmental*, vol. 101, no. 3-4, pp. 540–547, 2011.

[58] W. Shi, Y. Yan, and X. Yan, "Microwave-assisted synthesis of nano-scale BiVO4 photocatalysts and their excellent visible-light-driven photocatalytic activity for the degradation of ciprofloxacin," *Chemical Engineering Journal*, vol. 215-216, pp. 740–746, 2013.

[59] T. A. Gad-Allah, M. E. M. Ali, and M. I. Badawy, "Photocatalytic oxidation of ciprofloxacin under simulated sunlight," *Journal of Hazardous Materials*, vol. 186, no. 1, pp. 751–755, 2011.